Boundary Layer Mass, Water, and Heat Budgets in Wintertime Cold-Air Outbreaks from the Arctic Sea Ice

BURGHARD BRÜMMER

Meteorological Institute of the University of Hamburg, Hamburg, Germany

(Manuscript received 3 January 1996, in final form 25 September 1996)

ABSTRACT

Eleven cold-air outbreaks from the Arctic sea ice to the open water of the Fram Strait and the Norwegian Sea have been monitored by aircraft during the field campaigns ARKTIS 1991 and ARKTIS 1993.

Budgets of mass, water vapor, water, and heat in the atmospheric boundary layer are computed for boxes that are located at different distances from the ice edge ranging from the marginal ice zone to several hundred kilometers downstream.

Averaged over all cold-air outbreaks, the large-scale flow is divergent near the ice edge and convergent at larger distances from the ice edge. Regardless of divergence, the large-scale flow exports everywhere water vapor, water, and heat from an atmospheric box within the boundary layer. In the case of the water vapor budget this export and the loss by condensation in clouds are compensated by evaporation from the sea surface. Both the condensation in clouds and surface evaporation increase in downstream direction, as does their ratio from about 0.4 near the ice edge to about 0.8 at distances greater than 300 km.

In the water budget, the source by condensation in clouds is compensated by two sinks: large-scale flow export and precipitation. Precipitation increases absolutely from about 1–4 mm day^{-1} in downstream direction but the ratio of precipitation versus condensation remains approximately constant at a value of 0.75.

In contrast to the water vapor and water budgets with only one source, the heat budget has several sources, namely, surface heat flux, entrainment heat flux, condensation in clouds, and possibly radiation, which compensate for the heat export by the large-scale flow. The relative importance of these sources changes with distance from the ice edge. Near the ice edge, the surface heat flux at the first place and the entrainment flux at the second place are the relevant sources, while farther downstream in the region of deep convection—latent heat release by condensation is the dominating heat source. Here, the surface heat flux is of secondary importance and the entrainment flux plays a minor role.

Since a systematic transition from roll-like to cellular-like convection patterns is present in Arctic cold-air outbreaks, the differences in the budgets with respect to distance from the ice edge apply as well to the regions of rolls and cells, respectively. It is hypothesized that mesoscale cellular convection with cloud depths of more than 1 km does not occur unless the Bowen ratio is less than about 0.6.

1. Introduction

When cold air from the polar ice caps or from winterly continents is advected over adjacent open water, the atmospheric boundary layer is rapidly transformed with respect to its mean characteristics such as depth, temperature, water vapor, and liquid water content. Numerous studies on boundary layer modification and processes in cold-air outbreaks (CAOs) have been performed based on observations (e.g., Agee and Lomax 1978; Walter 1980; Walter 1986; Atlas et al. 1986; Wayland and Raman 1989; Chou and Zimmerman 1989; Brümmer et al. 1992) and numerical modeling (e.g., Stage and Businger 1981; Yuen 1985; Etling and Raasch 1987; Sun and Hsu 1988; Sun and Yildirim 1989; Bechthold et al. 1992; Chlond 1992).

In a recent paper, Brümmer (1996) described the boundary layer modification observed in 10 CAOs from the ice edges to the northwest and south of Spitzbergen during the field experiment ARKTIS in March 1993. In this field experiment, for the first time, not only the boundary layer modification over the open water could be measured, but also the initial conditions over the ice, the boundary conditions at the bottom and top of the boundary layer, and the conditions of the large-scale flow. The importance of these external conditions on the development of the internal boundary layer parameters could be demonstrated.

In this paper, estimates of the budgets of mass, water vapor, water, and heat in the atmospheric boundary layer at different distances from the ice edge during CAOs will be presented. The purpose is to quantifiy the individual processes that are responsible for the boundary layer modification, such as horizontal and vertical ad-

Corresponding author address: Dr. Burghard Brümmer, Meteorological Institute, University of Hamburg, Bundesstr. 55, D-20146 Hamburg, Germany.

© 1997 American Meteorological Society

Downloaded from http://journals.ametsoc.org/mwr/article-pdf/125/8/1824/4178812/1520-0493(1997)125_1824_blmwah_2_0_co_2.pdf by guest on 30 November 2020

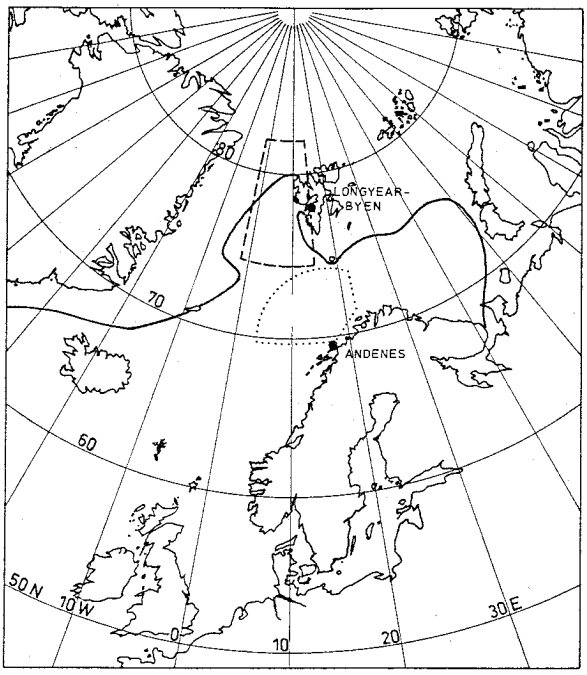

FIG. 1. Geographical location of the field experiments ARKTIS 1991 (dotted) and ARKTIS 1993 (dashed). Aircraft operation centers were Andenes and Longyearbyen, respectively. The full line marks the ice edge.

vection, surface and entrainment fluxes, radiation, condensation and precipitation, and to determine their relative importance in the budget at different stages of boundary layer development, that is, at different distances from the ice edge.

The cbudgets were calculated for eight of the abovementioned CAOs observed during ARKTIS 1993 (Brümmer 1993) and for three CAOs observed during a precursor experiment ARKTIS 1991 (Brümmer 1992) conducted over the northern part of the Norwegian Sea in February and March 1991. The areas of both field campaigns are shown in Fig. 1. The CAOs during ARKTIS 1993 were observed at distances between −30 km and about 300 km downstream from the ice edge, whereas those during ARKTIS 1991 were observed at greater distances—that is, 300 to 1000 km where the boundary layer development reached a more or less steady state.

Satellite images of CAOs show that the convection, as manifested by the appearance of clouds, is organized in characteristic patterns, beginning with streetlike patterns near the ice edge or coast and changing to cellular-like patterns at distances of several hundred kilometers farther downstream. There are theoretical and numerical considerations that suggest that the difference in the convection patterns is related to the different importance of physical processes in the atmospheric boundary layer, such as surface heat flux, entrainment flux, radiation, condensation, or to their different relative importance (e.g., Sheu and Agee 1977; Helfand and Kalnay 1983; Fiedler 1984; van Delden 1987; Müller 1995). Since these physical processes are quantified when calculating the heat and moisture budgets, the relation between physical processes and convection patterns will also be discussed in this paper.

2. Budget equations

The conservation equations for density ρ, specific water vapor q, water content l, and potential temperature θ read

$$\frac{\partial \rho}{\partial t} = -\frac{\partial}{\partial x}(\rho u) - \frac{\partial}{\partial y}(\rho v) - \frac{\partial}{\partial z}(\rho w). \tag{1a}$$

We use a Cartesian coordinate system x, y, z with the x axis pointing downstream along the direction,

$$\frac{\partial q}{\partial t} = -u\frac{\partial q}{\partial x} - v\frac{\partial q}{\partial y} - w\frac{\partial q}{\partial z} - \frac{\partial}{\partial z}w'q' - (c - e), \tag{1b}$$

$$\frac{\partial l}{\partial t} = -u\frac{\partial l}{\partial x} - v\frac{\partial l}{\partial y} - w\frac{\partial l}{\partial z} - \frac{\partial}{\partial z}w'l' + (c - e) - r, \tag{1c}$$

$$\frac{\partial \theta}{\partial t} = -u\frac{\partial \theta}{\partial x} - v\frac{\partial \theta}{\partial y} - w\frac{\partial \theta}{\partial z} - \frac{\partial}{\partial z}w'\theta' + \frac{L}{c_p}(c - e) + \frac{1}{c_p}\frac{\partial R}{\partial z}, \tag{1d}$$

of the mean boundary layer wind. The corresponding wind components are u, v, w, and t denotes the time. The net condensation/evaporation rate is $(c - e)$ and r is the precipitation rate. The net radiation flux R is given by $R = S\downarrow - S\uparrow + L\downarrow - L\uparrow$, where $S\downarrow$, $S\uparrow$, $L\downarrow$, $L\uparrow$ are the downward- and upward-directed shortwave and longwave radiation fluxes, respectively. Here, L is the latent heat of sublimation and c_p is the specific heat of dry air.

We assume stationarity and homogeneity in the crosswind y direction. Then, we multiply Eqs. (1b)–(1d) by ρ, substitute Eq. (1a) into Eqs. (1b)–(1d), and integrate (1a)–(1d) vertically from the surface ($z = 0$) to the top of the boundary layer ($z = h$). Denoting the vertical average by a tilde ($\tilde{}$), the integrated Eqs. (1a)–(1d) read

$$-\frac{\partial}{\partial x}(h\tilde{\rho}\tilde{u}) + (\rho u)_h\frac{\partial h}{\partial x} - (\rho w)_h = 0, \tag{2a}$$

Downloaded from http://journals.ametsoc.org/mwr/article-pdf/125/8/1824/4178812/1520-0493(1997)125_1824_blmwah_2_0_co_2.pdf by guest on 30 November 2020

$$-\frac{\partial}{\partial x}(h\tilde{\rho}\tilde{u}\tilde{q}) + (\rho uq)_h\frac{\partial h}{\partial x} - (\rho wq)_h + (\rho w'q')_o - (\rho w'q')_h - h\tilde{\rho}(\tilde{c} - \tilde{e}) = 0, \quad (2b)$$

$$-\frac{\partial}{\partial x}(h\tilde{\rho}\tilde{u}\tilde{l}) + (\rho ul)_h\frac{\partial h}{\partial x} - (\rho wl)_h + h\tilde{\rho}(\tilde{c} - \tilde{e}) - h\tilde{\rho}\tilde{r} = 0, \quad (2c)$$

$$-\frac{\partial}{\partial x}(h\tilde{\rho}\tilde{u}\tilde{\theta}) + (\rho u\theta)_h\frac{\partial h}{\partial x} - (\rho w\theta)_h + (\rho w'\theta')_o - (\rho w'\theta')_h + \frac{L}{c_p}h\tilde{\rho}(\tilde{c} - \tilde{e}) + \frac{1}{c_p}(R_h - R_o) = 0. \quad (2d)$$

In (2c) it has been assumed that the turbulent fluxes of liquid water, $(w'l')_o$ and $(w'l')_h$, can be neglected. We furthermore assumed in (2a)–(2d) that the vertically averaged transport $\widetilde{\rho ua}$ can be replaced approximately by $\tilde{\rho}\tilde{u}\tilde{a}$ where the variable a stands either for *1, q, l,* or θ.

Figure 2 illustrates the individual terms contributing to the budget of the variable a within an atmospheric boundary layer box. These are import and export of a by the mean flow through the vertical plane on the upwind and downwind side of the box, respectively, there is generally an import of a through the inclined top of the boundary layer. Depending on its sign, the mean vertical motion w_h causes either import or export. Furthermore, the variable a is changed by the surface flux, $(\rho'w'a')_o$, the entrainment flux, $(\rho w'a')_h$, and sources and sinks (condensation/evaporation, precipitation, radiation) within the box.

At the top h of the boundary layer there is often a sharp jump in θ, q, and l. Therefore, depending on the direction of the mean flow at h, the values of these variables have to be taken either from a level slightly above, h_+, or slightly below, h_-, when calculating the mean transport terms at h.

We are not able to calculate all terms in Eq. (2) directly from the measurements, which are described below. Therefore, some terms have to be calculated as residues. These terms are the vertical motion, $(\rho w)_h$, in (2a), the net condensation/evaporation, $h\tilde{\rho}(\tilde{c} - \tilde{e})$, in (2b), the precipitation, $h\tilde{\rho}\tilde{r}$, in (2c) and the entrainment flux, $(\rho w'\theta')_h$, in (2c). Beside the respective physical process, the residual terms thus also contain all uncertainties implied by the assumptions, the computational procedures, and the measurements. This has to be kept in mind when interpretating the budget results. Plausibility considerations, contraints, and comparisons of the individual CAOs with each other have to be taken into account in order to judge the validity of the results.

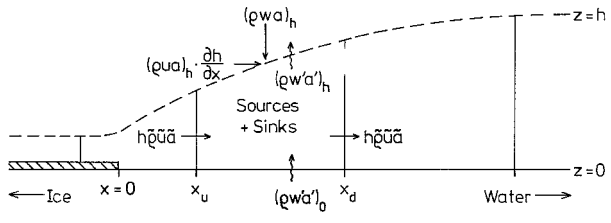

FIG. 2. Schematic presentation of the processes influencing the budget of the variable a within an atmospheric boundary layer box between the surface ($z = 0$) and the top ($z = h$) and the upstream (x_u) and downstream (x_d) vertical boundary. See text for explanation of other symbols.

3. The data

The data used in this study were sampled by two aircraft: a Falcon-20 and a Dornier-128. Both aircraft were equipped with gust probe systems to measure the mean values and turbulent fluctuations of θ, q, u, v, w, and pressure p at sample rates of 100 and 25 per second, respectively. The typical flight speeds were 100 and 60 m s^{-1}, respectively. The Falcon was additionally equipped with sensors to measure $S\downarrow$, $S\uparrow$, $L\downarrow$, and $L\uparrow$. Further details about the aircraft equipment can be found in Brümmer (1993).

Flight missions were carried out either as single missions of the Falcon or as joint missions of both aircraft. A typical flight pattern of a joint aircraft mission is sketched in Fig. 3. The pattern consisted of four vertical cross sections oriented perpendicular to the mean flow at different distances from the ice edge. Depending on the depth of the boundary layer, two to six horizontal flight legs of 30–50-km length were placed within a cross-sectional plane. Vertical profiles were flown at both sides of the vertical cross section. Furthermore, vertical profiles and horizontal legs were flown along the connections between the cross sections. In case of a single aircraft mission of the Falcon the flight pattern consisted of only three or two cross sections. The flight missions started from the airfield Longyearbyen on Spitsbergen during the ARKTIS 1993 campaign and from the airfield Andenes in north Norway during the ARKTIS 1991 campaign (see Fig. 1).

Intercomparison flights between Falcon and Dornier were performed during both campaigns. The differences concerning the mean values of θ, q, u, v, w, and p are presented in Brümmer (1992 and 1993) and were accounted for in the calculations made here. The differences (DORNIER minus FALCON) in the turbulent sensible heat fluxes, which amounted to -1 and $+6$ W m^{-2} or to -9% and $+15\%$ of the mean flux during the two campaigns, respectively, were not corrected for because—beside possible instrumental deficiencies—they may also be a consequence of sampling representativeness.

Downloaded from http://journals.ametsoc.org/mwr/article-pdf/125/8/1824/4178812/1520-0493(1997)125_1824_blmwah_2_0_co_2.pdf by guest on 30 November 2020

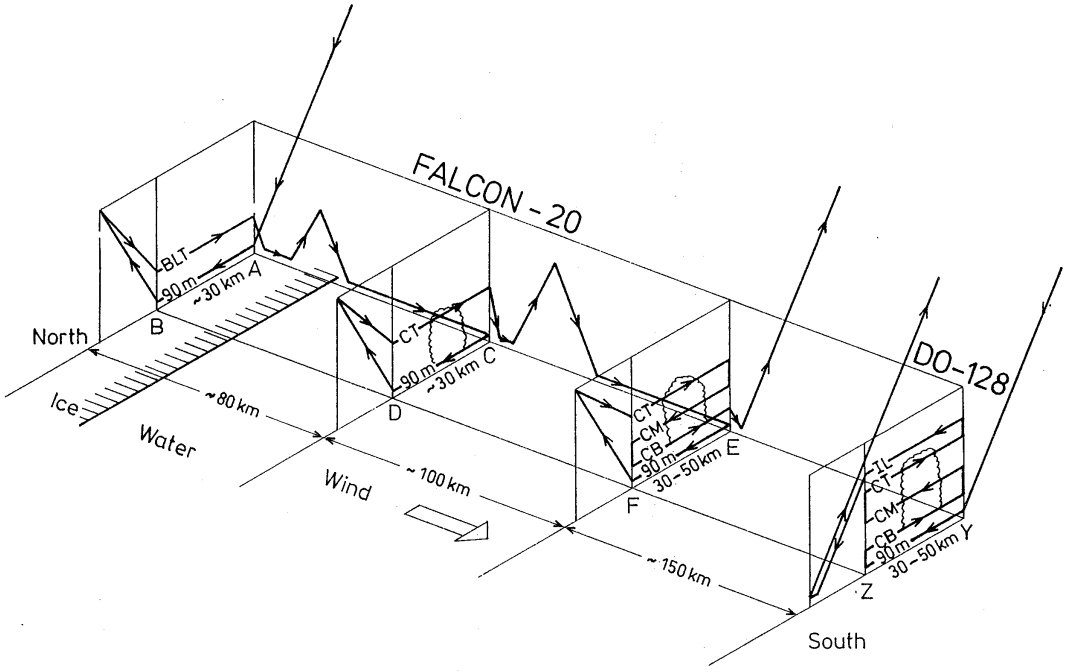

FIG. 3. Typical flight patterns of research aircraft Falcon-20 and Dornier-128 during a joint flight mission. The abbreviations BLT, 90 m, CB, CM, CT, IL stand for the level of the crosswind flight legs: boundary layer top, 90-m height, cloud base, cloud middle, cloud top, and inversion layer, respectively.

4. Computational procedure

From the vertical profiles at both sides of the vertical cross sections, the boundary layer depth h, the vertical averages $\tilde{u}$, $\tilde{q}$, $\tilde{l}$, $\tilde{\theta}$, and the corresponding values at levels h and $h + 50$ (50 m above h), that is, u_h, q_h, q_{h+50}, l_h, θ_h, and θ_{h+50}, were determined. It is assumed that $u_{h+50} = u_h$ and that $l_{h+50} = 0$. Depending on the direction of the mean flow, the values either at h or at $h + 50$ are used to calculate the terms $(\rho ua)_h$ $(\partial h/\partial x)$ and $(\rho wa)_h$ in Eqs. (2a)–(2d). The data from both profiles are then averaged and used as representative values for the corresponding cross section to determine the first three terms on the left-hand sides of Eqs. (2a)–(2d).

The water content l was not measured. Instead it was estimated assuming adiabatic conditions within the cloud whose base, h_{cb}, and top, h_{ct} $(= h)$, and coverage, N, were observed by the aircraft scientist. Thus, it is assumed

$$l = 0 \text{ at } z = h_{cb} \tag{3a}$$

$$l_h = l^{max} N \text{ at } z = h \tag{3b}$$

with $l^{max} = (dq_s/dp)\,(p_{cb} - P_h)$, where q_s is the saturation specific humidity. The water content $\tilde{l}$, averaged over the depth of the boundary layer, was calculated according to

$$\tilde{l} = \frac{1}{2} l^{max} N \left(\frac{h_{ct} - h_{cb}}{h} \right). \tag{4}$$

Due to the assumption of adiabatic conditions, $\tilde{l}$ and l_h may be slightly overestimated. The surface fluxes of moisture, $(\rho w' q')_o$, and temperature, $(\rho w' \theta')_o$, were determined by extrapolation of the corresponding flux measurement from the horizontal flight leg at the lowest allowable flight level of 90 m down to the surface applying the gradient between 90 m and the flux measurements at other flight levels. In this way, $(\rho w' \theta')_o$ resulted in values that are about 10% larger than $(\rho w' \theta')_{90}$, while $(\rho w' q')_o$ and $(\rho w' q')_{90}$ are not much different.

The radiation flux difference $R_h - R_o$ was calculated from the mean values of $S\downarrow$, $S\uparrow$, $L\downarrow$, and $L\uparrow$ measured at 90 m and at a flight level near cloud top. Since the radiation fluxes $S\downarrow$, $S\uparrow$, $L\downarrow$, and $L\uparrow$ depend strongly on cloud coverage and since a horizontal flight leg may not be representative with respect to cloud cover, a second method to estimate R_o and R_h was applied. For this method those parts of a flight leg were selected that are representative for the radiation fluxes under cloudy ($S\downarrow_c$, $S\uparrow_c$, $L\downarrow_c$, $L\uparrow_c$) and open conditions ($S\downarrow_o$, $S\uparrow_o$, $L\downarrow_o$, $L\uparrow_o$) and were then weighted by cloud coverage N and noncloud coverage $(1 - N)$, respectively. For a level directly above cloud top we calculate

$$R_h = N\,(S\downarrow_o - S\uparrow_c + L\downarrow_o - L\uparrow_c) + (1 - N)(S\downarrow_o - S\uparrow_o + L\downarrow_o - L\uparrow_o), \tag{5a}$$

and for the 90-m level we calculate

Downloaded from http://journals.ametsoc.org/mwr/article-pdf/125/8/1824/4178812/1520-0493(1997)125_1824_blmwah_2_0_co_2.pdf by guest on 30 November 2020

$$R_o = N(S\downarrow_c - S\uparrow_c + L\downarrow_c - L\uparrow_o) + (1 - N)(S\downarrow_o - S\uparrow_o + L\downarrow_o - L\uparrow_o), \quad (5b)$$

assuming that $R_o \approx R_{90}$.

The individual terms of the budget equations (2a)–(2d) were then computed in the following sequence. First, (2a) is computed with the term $(\rho w)_h$ as residual. Then, using $(\rho w)_h$, (2b) is solved with the term $h\tilde{\rho}(\tilde{c} - \tilde{e})$ as residue. Finally, using $(\rho w)_h$ and $h\tilde{\rho}(\tilde{c} - \tilde{e})$, (2c) and (2d) are solved with the terms $h\tilde{\rho}\tilde{r}$ and $(\rho w'\theta')_h$ as residues, respectively.

The residual terms in each equation, of course, contain all uncertainties of the other terms that may originate from instrumental errors, computational uncertainties, unrepresentative sampling, or other sources. The results of the computations therefore have to be interpreted with great care and—since exact figures on the accuracy (for example, representativeness of the sampling) cannot be given—have to be assessed by comparison of similar and different cases, physical constraints, and other criteria.

Flight legs of 30–50-km length in open cellular convection with 10–30-km cell diameters are probably not long enough to cover open and cloudy areas in a representative manner. Brümmer et al. (1986) distinguished flux measurements in open cellular convection with respect to cloudy and open subareas. They found for 90-m height that the sensible heat fluxes in cloudy and open areas deviated from the mean value by about +15% and −15%, respectively, and that the latent heat fluxes deviated by about ±5%. Thus, concerning representativeness of the flux measurements in open cellular convection the possible errors cannot be too large. If, for example, open and cloudy areas cover in reality 0.5 of the total area, but the flight track intersects, say, 0.7 cloudy and 0.3 open areas, the sensible heat flux has an error of 6% and the latent heat flux of 2%.

5. Results of the budget calculations

a. Mean values used in the budget calculations

As mentioned above, boundary layer budgets were calculated for eight cold-air outbreaks observed during the field campaign ARKTIS 1993 and for three cold-air outbreaks observed during ARKTIS 1991. The relevant boundary layer parameters characterizing the structure of the boundary layer and entering into the budget computations are listed in Table 1. They were determined from the aircraft measurements and represent average values for the vertical cross sections oriented perpendicular to the mean flow as sketched in Fig. 3.

The observations cover a wide range of distances x reaching from the ice (in all ARKTIS 1993 cases) to more than 1000 km downstream (ARKTIS 1991) and a wide range of atmospheric boundary layer conditions. In all cases, the depth h, the specific humidity $\tilde{q}$, and potential temperature $\tilde{\theta}$ of the boundary layer increased downstream. The rate of increase depends to a large degree on the static stability of the air above the boundary layer as already described in Brümmer (1996). When the stability, as represented in Table 1 by the potential temperature increase $\Delta\theta_{50}$ over 50-m-thick layer above h, is large, h increases slowly (as, for example, on 16, 19, 20, and 24 March 1993) and vice versa. The temperature difference $\Delta\theta_{50}$ generally becomes smaller with increasing distance x. The stability above deep boundary layers as, for example, on 10 March 1993 and 7 and 8 March 1991 is usually relatively small. On the other hand, the growth rate of boundary layer depth h has consequences on the layer averages $\tilde{q}$ and $\tilde{\theta}$, because the moisture and heat supplied from the sea surface is then distributed over a layer of different depth.

Cloud amount, as represented by cloud coverage N, cloud layer depth Δh_{cloud}, and cloud water content $\tilde{l}$, also increased generally in downstream direction, suggesting an increasing importance of the condensation process on the boundary layer development. This is supported below by the results of the budget calculations. The deepest cloud layers with depths of more than 1000 m were observed with the deepest boundary layers on 10 March 1993 and 7 and 8 March 1991. Shallow cloud and boundary layers were present in the CAOs on 16, 19, 20, and 24 March 1993. The CAOs on 5, 11, and 25 March 1993, and 24 February 1991 represent cases with intermediate moderate cloud activity.

The observed cold-air outbreaks occurred with wind speeds $\tilde{u}$, which ranged from 4 to 14 m s^{-1} over the ice and increased generally in downstream direction. On 20 March 1993, an average boundary layer wind speed of more than 20 m s^{-1} was observed at the second cross-wind vertical plane. Since wind speed determines to a large degree the magnitude of the sea–air heat and moisture fluxes, it is of considerable importance for the heat and moisture budget of the boundary layer, as can be seen below in Tables 3 and 5. On the other hand, the data in Table 1 for the eleven CAOs show that the influence of the wind and thus the surface heat fluxes on the growth of the boundary layer depth is small compared, for example, to the influence exerted by the static stability of the air on top of the boundary layer.

b. Mass budget

The results of the mass budget calculations are summarized in Table 2. Despite a high degree of variability in the mass budget from one CAO to the other, two features are more or less the same for all cases. The first feature is a net export of mass by the horizontal flow through the vertical planes oriented perpendicular to the wind. This is true for 16 out of the 22 budget boxes due to the downstream increase of h and $\tilde{u}$. Only in those cases when either h (10 March 1993) or $\tilde{u}$ (19 and 20 March 1993; 24 February and 8 March 1991) decreased is there a net mass import. The second feature is, except for the fourth box on 10 March 1993, a substantial horizontal import of mass through the inclined

Downloaded from http://journals.ametsoc.org/mwr/article-pdf/125/8/1824/4178812/1520-0493(1997)125_1824_blmwah_2_0_co_2.pdf by guest on 30 November 2020

TABLE 1. Average boundary layer conditions for vertical planes perpendicular to the wind (as sketched in Fig. 2) at different distances x from the ice edge for eight cold-air outbreaks during ARKTIS 1993 and three cold-air outbreaks during ARKTIS 1991. The Δh_{cloud} is the cloud-layer depth, Δq_{50} and $\Delta\theta_{50}$ are the differences of q, and θ over a 50-m-deep layer above the top h of the boundary layer. See text for explanation of other symbols.

	x	h	Δh_{cloud}	N	$\tilde{u}$	u_h	$\tilde{q}$	q_h	Δq_{50}	$\tilde{l}$	l_h	$\tilde{\theta}$	θ_h	$\Delta\theta_{50}$
Date	(km)	(m)		(octa)	(m s^{-1})		(g kg^{-1})					(°C)		(K)
5 Mar 93	−38	345	75	1.3	5.3	5.8	0.56	0.53	−0.09	0	0	−21.6	−21.0	0.4
	27	590	280	4.5	7.2	6.9	0.67	0.53	−0.16	0.02	0.06	−17.3	−16.9	1.3
	125	1285	755	6	7.2	5.4	0.79	0.61	−0.15	0.07	0.23	−13.0	−12.4	1.0
10 Mar 93	−40	260	180	2	5.8	5.2	0.16	0.15	0.01	0	0.08	−30.7	−29.9	1.3
	47	720	520	6	9.6	7.5	0.32	0.23	0.01	0.07	0.18	−22.5	−22.2	1.0
	148	1440	1230	6.5	6.0	5.0	0.36	0.19	−0.01	0.16	0.37	−17.8	−17.3	0.8
	271	2085	1460	5.5	4.1	4.0	0.42	0.17	−0.02	0.13	0.38	−14.3	−13.7	1.2
	445	1975	1400	5.5	1.7	0.7	0.58	0.22	−0.03	0.16	0.45	−11.5	−10.8	0.6
11 Mar 93	−83	295	0	0	4.5	4.7	0.36	0.32	−0.16	0	0	−24.7	−24.6	1.6
	26	700	410	5.5	3.9	3.3	0.60	0.43	−0.11	0.03	0.11	−18.0	−17.9	0.9
	111	1155	660	6	4.4	4.5	0.68	0.55	−0.06	0.05	0.19	−14.3	−13.9	0.7
16 Mar 93	−40	215	75	8	6.7	4.9	0.47	0.53	0.12	0.01	0.03	−21.7	−20.9	4.1
	54	450	295	8	5.4	5.1	0.97	0.90	0.17	0.06	0.19	−13.9	−13.5	3.9
	171	780	470	8	5.2	2.7	1.27	1.13	0.16	0.11	0.35	−8.7	−8.1	4.5
19 Mar 93	−30	240	240	1	13.3	13.8	0.23	0.28	0.07	0	0.08	−27.3	−26.1	5.2
	53	555	255	8	13.8	11.9	0.71	0.69	0.14	0.02	0.08	−17.3	−16.5	3.9
	173	780	455	7	8.5	6.6	1.22	1.04	−0.07	0.06	0.21	−10.2	−9.4	2.2
20 Mar 93	−43	200	200	1.2	10.8	11.3	0.22	0.20	−0.02	0	0.01	−29.6	−29.2	1.8
	40	375	315	4.3	20.9	20.2	0.59	0.44	−0.15	0.03	0.06	−18.9	−18.7	3.3
	150	490	305	5	13.1	12.8	1.30	1.12	−0.68	0.04	0.13	−10.2	−10.0	3.2
24 Mar 93	−40	195	0	0	9.4	10.6	0.22	0.24	0.05	0	0	−30.5	−30.3	4.2
	56	390	260	5.1	15.0	14.4	0.71	0.60	−0.08	0.03	0.08	−18.3	−17.9	3.3
	172	635	430	5.8	15.1	14.7	1.14	0.94	−0.36	0.07	0.21	−11.2	−10.7	2.4
25 Mar 93	−23	200	100	1	7.4	7.8	0.39	0.39	−0.01	0	0	−25.7	−25.6	1.1
	61	740	615	6	10.8	11.1	0.59	0.50	−0.04	0.09	0.22	−17.7	−17.2	1.9
	172	1045	840	6	14.1	13.6	0.86	0.74	−0.17	0.14	0.34	−13.5	−12.8	2.4
	310	1140	800	7	16.4	16.0	1.09	0.65	−0.29	0.15	0.42	−10.1	−9.5	1.2
24 Feb 91	100	1455	875	6	9.5	6.7	1.78	1.33	−0.52	0.11	0.37	−2.6	−1.5	1.8
	192	1505	800	5	7.0	4.8	1.87	1.53	−0.20	0.09	0.32	−1.0	0.2	1.1
7 Mar 91	600	1200	425	4.5	15.6	16.7	2.10	1.78	−0.30	0.03	0.16	−1.8	−1.3	0.7
	850	2130	1260	4	12.3	12.5	1.90	1.10	−0.20	0.12	0.40	1.0	2.7	0.6
8 Mar 91	1000	2600	2075	4	7.9	5.1	1.37	0.68	−0.10	0.29	0.74	−1.9	0.6	0.1
	1150	2700	1950	4	7.4	8.0	1.50	0.95	−0.35	0.24	0.68	−0.2	2.3	0.9

top of the boundary layer. Mostly of opposite sign, both horizontal flow terms sum up to different signs and magnitudes of the mean vertical mass flux. This is not true for those budget boxes during ARKTIS 1993, which are situated around the ice edge ($x = 0$). Here, subsidence is calculated in five of eight CAOs and in the other three cases $(\rho w)_h$ is nearly zero. This is probably a consequence of the strong ice–sea temperature contrast of 20–30 K and the resulting ice–sea breeze, which is superimposed on the synoptic flow. The largest downstream acceleration was observed on 20 March 1993 when $\tilde{u}$ increased from 10.8 to 20.9 m s^{-1} within a distance of 83 km. This led to a mean subsidence w_h of about −0.03 m s^{-1} at 300-m height.

Consistent with the general view of the generation of deep convection, a mean upward mass flux $(\rho w)_h$ is calculated as residue in those three CAOs (10 March 1993, 7 and 8 March 1991) when the convective activity was strong with a deep cloud and boundary layer. At the top of the boundary layer, at levels of more than 2 km, w_h results into values between 0.01 and 0.03 m s^{-1}.

Equation (2a) for the mass budget of the boundary layer is identical with the well-known balance equation for the top of the boundary layer h usually written in the form (e.g., Stull 1988):

$$\frac{dh}{dt} - w_e - \bar{w} = 0. \tag{6}$$

Under the assumptions made above (stationarity and homogeneity in the crosswind direction), dh/dt is represented by $u_h(\partial h/\partial x)$ and the entrainment velocity w_e by

$$w_e = \frac{1}{\rho_h}\frac{\partial}{\partial x}(h\tilde{\rho}\tilde{u}). \tag{7}$$

Since ρ_h is about 10^3 gm^{-3}, the numerical values of $\partial(h\tilde{\rho}\tilde{u})/\partial x$ in Table 2 approximately represent w_e in units of millimeters per second. As already mentioned above, $\partial(h\tilde{\rho}\tilde{u})/\partial x$ is positive in 16 out of 22 budget boxes; that is, air is entrained from the inversion layer into the boundary layer. This holds for all budget boxes situated around the ice edge ($x = 0$) where h increases rapidly. On the other hand, $\partial(h\tilde{\rho}\tilde{u})/\partial x$ is negative; that is, air is detrained from the boundary layer in those cases where

Downloaded from http://journals.ametsoc.org/mwr/article-pdf/125/8/1824/4178812/1520-0493(1997)125_1824_blmwah_2_0_co_2.pdf by guest on 30 November 2020

TABLE 2. The individual terms of the mass budget [Eq. (2a)] for 11 cold-air outbreaks measured during the field campaigns ARKTIS 1993 and ARKTIS 1991. Here, x_u and x_d represent the position (relative to the ice edge) of the upstream and downstream vertical plane of the box between which the budget is calculated. Positive and negative values of the budget terms refer to mass import and mass export, respectively. The term $-(\rho w)_h$ was calculated as residue.

Date	x_u/x_d (km)	$-\frac{\partial}{\partial x}(h\tilde{\rho}\tilde{u})$	$(\rho u)_h\frac{\partial h}{\partial x}$	$-(\rho w)_h$	w_h (m s^{-1})
		(g m^{-2} s^{-1})			
5 March 1993	−38/27	−49	32	17	−0.013
	27/125	−61	54	7	−0.006
10 March 1993	−40/47	−82	45	37	−0.028
	47/148	−17	55	−38	0.031
	148/271	4	27	−31	0.027
	271/445	37	−2	−35	0.032
11 March 1993	−83 26	−16	19	−3	0.003
	26/111	−33	26	7	0.006
16 March 1993	−40/54	−13	16	−3	0.003
	54/171	−17	14	3	−0.003
19 March 1993	−30/53	−65	65	0	−0.000
	53/173	13	22	−35	0.028
20 March 1993	−43/40	−91	45	46	−0.033
	40/150	21	23	−44	0.033
24 March 1993	−40/56	−55	34	21	−0.015
	56/172	−38	39	−1	0.001
25 March 1993	−23/61	−101	80	21	−0.016
	61/172	−75	42	33	−0.027
	172/310	−33	12	21	−0.017
24 February 1991	100/192	45	4	−49	0.038
7 March 1991	600/850	−31	61	−30	0.027
8 March 1991	1000/1150	6	5	−11	0.010

h decreases or $\tilde{u}$ decelerates. Interestingly, in all of these latter cases an upward motion, w_h, is calculated. However, the reverse is not true, that is, not in all cases of positive w_h is the entrainment velocity w_e negative.

The six detrainment cases are difficult to understand physically: under the conditions of positive w_h and decaying mechanical turbulence (decreasing $\tilde{u}$) in downstream direction air from the turbulent boundary layer invades into the non- or less-turbulent inversion layer. If the analysis $w_e < o$ is correct, more of the invaded air must remain in the inversion layer than is recycled together with inversion layer air into the boundary layer as is the case in the usual entrainment process. In the six cases, w_h moves the inversion base h upward at a rate [term $(\rho w)_h$ in Table 2] that is larger than or at least similar to the net effect of mass detrainment of turbulent air into the inversion layer [term $-\partial(h\tilde{\rho}\tilde{u})/\partial x$] so that the detrained air remains effectively in the boundary layer.

Taken together, the results for the mass budget within the 22 budget boxes appear to be plausible and support the confidence in the accuracy of the budget estimates.

c. Water vapor budget

The results of the water vapor budget calculations are compiled in Table 3. The horizontal flow through the crosswind vertical planes of the budget box results in a net export of q, except for 10 March 1993 and 24 February 1991. On these days the mean flow $\tilde{u}$ decelerated substantially and h decreased (10 March) or slightly increased (24 February) in downstream direction. The horizontal flow through the tilted top of the boundary layer, of course, always imports water vapor, while the vertical motion, depending on its sign, imports or exports q. In all cases the net effect of the mean flow results in a loss of q, which is listed in the column ''sum'' in Table 3. This loss is by far overcompensated by the supply of q from the sea surface. Turbulent transport of q through the top of the boundary layer is small. Usually this term, $-(\rho w'q')_h$, should be slightly negative, as was observed on 24 and 25 March 1993. However, on 16 and 19 March 1993, when q increased above the boundary layer (see Table 1) a downward turbulent moisture flux was measured. In the other cases, when no measurements were available, a vanishing flux $(w'q')_h$ was assumed.

The residual term in the water vapor budget, $h\tilde{\rho}(\tilde{c} - \tilde{e})$, is always positive; that is, in all cases there is a loss of water vapor due to a net transition from the vapor to the liquid or solid water phase. In all ARKTIS 1993 cases this net condensation increases in downstream direction. This appears to be plausible, also in the light of the water budget results presented in Table 4, and is regarded as an indicator for the validity of the budget estimates.

d. Water budget

Temperatures measured in the clouds were mostly between −15° and −30°C for the ARKTIS 1993 cases

Downloaded from http://journals.ametsoc.org/mwr/article-pdf/125/8/1824/4178812/1520-0493(1997)125_1824_blmwah_2_0_co_2.pdf by guest on 30 November 2020

TABLE 3. As in Table 2 but for the water vapor budget [Eq. (2b)]. The column ''sum'' is the sum of the first three budget terms representing the effects of the mean flow. Values for the term $(\rho w'q')_h$, represented by ~0, mean that no data were available and that a vanishing moisture flux at boundary layer top h was assumed. The term, $-h\tilde{\rho}(\tilde{c} - \tilde{e})$, was calculated as residue. Multiplying the numerical values in this table by the latent heat of sublimation L, the more familiar units watts per square meter result.

Date	$-\frac{\partial}{\partial x}(h\tilde{\rho}\tilde{u}\tilde{q})$	$(\rho uq)_h \frac{\partial h}{\partial x}$	$-(\rho wq)_h$	Sum	$(\overline{\rho w'q'})_o$	$-(\overline{\rho w'q'})_h$	$-h\tilde{\rho}(\tilde{c} - \tilde{e})$
				(10^{-3} g m^{-2} s^{-1})			
5 March 1993	−37	13	7	−17	20	~0	−3
	−55	22	3	−30	40	~0	−10
10 March 1993	−30	9	7	−14	43	~0	−29
	−10	12	−8	−6	73	~0	−67
	−4	5	−6	−5	60	~0	−55
	11	−0	−7	4	37	~0	−41
11 March 1993	−14	4	−1	−11	25	~0	−14
	−26	11	3	−12	37	~0	−25
16 March 1993	−23	14	−3	−12	19	3	−10
	−29	15	4	−10	28	5	−23
19 March 1993	−73	36	0	−37	53	3	−19
	−26	19	−30	−37	61	5	−29
20 March 1993	−67	11	11	−45	65	~0	−20
	−41	8	−34	−67	100	~0	−33
24 March 1993	−52	11	8	−33	52	−13	−6
	−74	22	−1	−53	82	−14	−15
25 March 1993	−65	34	9	−22	44	−10	−12
	−91	22	17	−52	79	−9	−18
	−68	5	10	−53	108	−6	−49
24 February 1991	68	4	−70	2	40	~0	−42
7 March 1991	−40	75	−43	−8	68	~0	−60
8 March 1991	−12	3	−9	−18	49	~0	−31

and between −7° and −10°C in the ARKTIS 1991 cases. We assume that water vapor is directly converted to ice and vice versa for temperatures below −15°C (see Curry et al. 1990). This assumption does not affect the water vapor and water budget but does affect the temperature budget presented in the following section, where L is either assumed as 2800 W s (g K)$^{-1}$ or as 2500 W s (g K)$^{-1}$.

The results of the water budget calculations are compiled in Table 4. The net condensation rate $h\tilde{\rho}(\tilde{c} - \tilde{e})$, calculated as residue from Eq. (2b), is—with one exception—the only source for water. The exception is the CAO on 19 March 1993 when clouds were advected with southerly winds in the stable layer above the boundary layer. In this case, water was imported by the mean horizontal flow through the inclined top of the boundary layer, but at a much smaller rate as was generated by condensation.

The net effect of all three processes related to the mean flow (listed in the column ''sum'' in Table 4) is always a sink of water. The main contributions arise from the divergence of the horizontal flow through the vertical planes of the budget box and from mean upward motion through the top of the boundary layer. The latter process is the only large-scale sink on 10 March 1993, 24 February, and 8 March 1991 when either the mean flow $\tilde{u}$ decelerated or the cloud amount (cloud depth, cloud average) decreased in downstream direction (see Table 1).

To balance the water budget within the budget box, precipitation is needed in all CAO cases. According to the observations by the aircraft scientists, precipitation was indeed present in all cases. However, precipitation was not measured qualitatively but judged by eye. It was observed that the precipitation ''intensity'' increased downstream, as is the case for the residual term $-h\rho\tilde{r}$ in all ARKTIS 1993 CAOs. A value of 10^{-3} g (m^2 s)$^{-1}$ corresponds to a precipitation rate of about 1.1 mm day^{-1}. The precipitation is largest with 4–5 mm day^{-1} in those cases with large Δh_{cloud}, that is, when the convective cloud activity is strong to moderate, as for example on 10 and 25 March 1993 or in the ARKTIS 1991 cases. These precipitation rates compare well with values of up to 8 mm day^{-1} observed in mesoscale cellular convection in CAO over the East China Sea (Ninomiya and Akiyama 1976).

The fact that no ''negative precipitation'' is calculated as residue in the water budget is not a self-evident result considering error possibilities and thus can again be regarded as an indication that the budget results are at least qualitatively true.

The relatively large precipitation values diagnosed in the first budget box for 19 and 20 March 1993 are probably not correct and presumably by about 10×10^{-3} g (m^2 s)$^{-1}$ too large compared to the precipitation rates diagnosed on 16 and 24 March 1993 with otherwise rather similar characteristics of the boundary layer (see Table 1). This may be regarded as a possible measure for the uncertainty of the water budget residue in general. On the other hand, at least on 19 March 1993

Downloaded from http://journals.ametsoc.org/mwr/article-pdf/125/8/1824/4178812/1520-0493(1997)125_1824_blmwah_2_0_co_2.pdf by guest on 30 November 2020

TABLE 4. As in Table 3 but for the water budget [Eq. (2c)]. The term $-h\tilde{\rho}\tilde{r}$ was calculated as residue.

Date	$-\frac{\partial}{\partial x}(h\tilde{\rho}\tilde{l})$	$(\rho u l)_h \frac{\partial h}{\partial x}$	$-(\rho w l)_h$	Sum	$h\tilde{\rho}(\tilde{c} - \tilde{e})$	$-h\tilde{\rho}\tilde{r}$
	(10^{-3} g m^{-2} s^{-1})					
5 March 1993	−1	0	0	−1	3	−2
	−7	0	0	−7	10	−3
10 March 1993	−7	0	0	−7	29	−22
	−11	0	−10	−21	67	−46
	3	0	−12	−9	55	−46
	4	−1	−14	−11	42	−31
11 March 1993	−1	0	−0	−1	14	−13
	−3	0	0	−3	25	−22
16 March 1993	−2	0	−0	−2	10	−8
	−3	0	0	−3	23	−20
19 March 1993	−2	1	0	−1	19	−18
	−3	1	−5	−7	29	−22
20 March 1993	−3	0	0	−3	20	−17
	−1	0	−4	−5	33	−28
24 March 1993	−2	0	0	−2	6	−4
	−6	0	−0	−6	15	−9
25 March 1993	−11	0	0	−11	12	−1
	−11	0	0	−11	18	−7
	−9	0	0	−9	49	−40
24 February 1991	9	0	−17	−8	42	−34
7 March 1991	−12	0	−9	−21	60	−39
8 March 1991	9	0	−7	2	31	−33

when—as mentioned above—clouds were also present on top of the boundary layer, it cannot be excluded that precipitation particles from that layer fell through the boundary layer clouds and collected and removed cloud water.

e. Potential temperature budget

The results of the computations for the potential temperature budget are summarized in Table 5. As for the budgets of water vapor and water, the net effect of the

TABLE 5. As in Table 3 but for the potential temperature budget [Eq. (2d)]. The term $(\rho w'\theta')_h$ was calculated as residue. Multiplying the numerical values in this table by the specific heat c_p, the more familiar units watts per square meter result.

Date	$-\frac{\partial}{\partial x}(h\tilde{\rho}\tilde{u}\tilde{\theta})$	$(\rho u\theta)_h \frac{\partial h}{\partial x}$	$-(\rho w\theta)_h$	Sum	$(\rho w'\theta')_o$	$-(\rho w'\theta')_h$	$\frac{L}{c_p} h\tilde{\rho}(\tilde{c} - \tilde{e})$	$\frac{1}{c_p}(R_h - R_o)$
	(g K m^{-2} s^{-1})							
5 March 1993	−12 701	8093	4429	−179	93	64	9	13
	−16 239	14 101	1839	−299	141	112	25	21
10 March 1993	−20 769	11 150	9245	−374	93	206	82	−7
	−4874	14 085	−9663	−452	145	133	189	−15
	804	7038	−8126	−284	112	60	138	−26
	9446	−426	−9162	−143	99	−14	104	−46
11 March 1993	−4271	4983	−867	−155	110	16	40	−11
	−8750	6693	1879	−178	127	10	61	−20
16 March 1993	−3442	4231	−924	−135	82	28	29	−4
	−4594	3641	837	−116	100	−37	57	−4
19 March 1993	−17 195	16 606	35	−554	261	190	54	49
	2943	5728	−9183	−512	248	135	72	57
20 March 1993	−23 509	11 410	11 546	−553	262	243	57	−9
	4671	5872	−11 254	−711	362	299	84	−34
24 March 1993	−14 339	8719	5208	−412	210	176	17	9
	−10 524	10 302	−285	−507	291	165	38	13
25 March 1993	−26 049	20 378	5307	−364	219	122	35	−12
	−20 007	11 011	8657	−339	281	30	46	−18
	−9223	3284	5568	−371	275	−7	123	−20
24 February 1991	12 054	969	−13 333	−310	106	98	106	~0
7 March 1991	−8618	16 632	−8257	−243	77	21	150	−5
8 March 1991	1396	1233	−2908	−279	79	122	78	~0

Downloaded from http://journals.ametsoc.org/mwr/article-pdf/125/8/1824/4178812/1520-0493(1997)125_1824_blmwah_2_0_co_2.pdf by guest on 30 November 2020

TABLE 6. Grouping of the 22 budget boxes during the 11 days of CAOs with respect to their distance from the ice edge. The last column gives the total number of budget boxes within each group. The letters within the table refer to the type of convective cloud pattern: R—rolls, C—cells.

Distance from ice edge	Day of March 1993								Day of February/March 1991			
	5	10	11	16	19	20	24	25	24	7	8	Number
Around ice edge	R	R	R	R	R	R	R	R				8
30–150 km	R/C	R/C	R/C	R	R	R	R	R				8
150–30 km		R/C						R/C	R/C			3
>300 km		C								C	C	3

three terms related to the mean flow (listed in the column ''sum'' in Table 5) is negative—that is, a cooling of the boundary layer. As for the other budgets, this is caused either by the divergence of the horizontal flow through the vertical crosswind planes of the budget box or by the mean vertical motion through the top of the boundary layer, while the horizontal flow through the tilted top always represents a warming. However, in contrast to the other budgets, the net effect of the large-scale terms is about one order of magnitude smaller than the individual terms themselves. Consequently, the error source for the term ''sum,'' as a small difference between large values, is larger than in the case of the water vapor and water budget.

The heat loss caused by the mean flow is compensated by the surface heat flux, the entrainment flux, net condensation, and partly by the radiation flux difference. The surface heat flux is mostly the largest source term. It increases from the area over the ice (values around 20 W m^{-2}) toward the open water and decreases slowly farther downstream due to the decreasing sea–air temperature difference. Details are given in Brümmer (1996). As mentioned above, the net condensation is a heat source that increases in downstream direction with respect to magnitude and relative importance compared to the other source terms. This will be discussed further in section 6.

The radiation flux divergence can be a heat source or heat sink as well. It depends on the cloud conditions and on the time of day. All flight missions here were flown during daytime around noon, except the missions in the CAOs on 20 March 1993 and 24 February 1991, which were flown in the later afternoon. Due to the unknown representativeness of the actual flight track with respect to the cloud field, the radiation term bears some uncertainty. This can be concluded from comparisons of the two methods described in section 4 to calculate this term. The estimates between both methods can differ by ± 20 g K $(m^2\ s)^{-1}$.

The entrainment heat flux was calculated as residue and, of course, contains all uncertainties originating from the other terms. Nevertheless, the results are not unreasonable. A downward entrainment heat flux is diagnosed in 19 out of 22 budget boxes. Only in three cases an upward entrainment flux is diagnosed that is physically not consistent with the temperature increase $\Delta\theta_{50}$ (see Table 1), which was also present in these cases. Since $(\rho w'\theta')_h$ should not fall short of the lower limit of zero, we can use the three unrealistic values to obtain an estimate for the uncertainty of this term: it is probably on the order of ± 50 g K $(m^2\ s)^{-1}$. Another constraint to judge the validity of the results is that the entrainment flux $-(\rho w'\theta')_h$ should not be much larger than $(\rho w'\theta')_o$ because the turbulent kinetic energy needed for entrainment is predominantly supplied by the surface buoyancy flux, which itself is predominantly given by the surface sensible heat flux. With respect to this second constraint, the entrainment flux values are relatively reasonable (except for the first budget box on 10 March 1993). This and also the fact that the entrainment flux decreases in general in downstream direction in accordance with the decreasing temperature difference $\Delta\theta_{50}$ on top of the boundary layer gives further confidence in the temperature budget results in general, of course, not in each detail. Further, more general aspects of the budget results are discussed in section 6.

6. Budget results in relation to ice-edge distance and convective patterns

In this section the results of the budget calculations, which were performed for 22 individual budget boxes during 11 CAOs, are grouped with respect to the distance from the ice edge ($x = 0$). The idea behind this procedure is that general and systematic variations come out in a clearer way because natural variations as well as the unsystematic uncertainties inherent in the individual budget calculations presumably cancel out to some extent. The grouping with respect to the distance x from the ice edge is listed in Table 6. The table contains the grouping into four distance intervals and a classification of each budget box with respect to the dominating convective pattern observed within it: longitudinal roll-like structures, cellular structures, or transitional structures from rolls to cells. It can be seen that the grouping with respect to x goes parallel with the systematic pattern transition from rolls to cells.

a. Composite budgets

The results of the composite budgets are summarized in Table 7. When assessing the results it should be taken

Downloaded from http://journals.ametsoc.org/mwr/article-pdf/125/8/1824/4178812/1520-0493(1997)125_1824_blmwah_2_0_co_2.pdf by guest on 30 November 2020

TABLE 7. Budgets of mass, water vapor, water, and potential temperature composited with respect to distance from ice edge according to the classification given in Table 6.

	$-\frac{\partial}{\partial x}(h\tilde{\rho}\tilde{u}\tilde{u})$	$(\rho u)_h\frac{\partial h}{\partial x}$	$-(\rho w)_h$					
	(g m^{-2} s^{-1})							
Around ice edge	−59	42	17					
30–150 km	−26	34	−8					
150–300 km	5	14	−19					
>300 km	4	21	−25					
	$-\frac{\partial}{\partial x}(h\tilde{\rho}\tilde{u}\tilde{q})$	$(\rho uq)_h\frac{\partial h}{\partial x}$	$-(\rho wq)_h$	Sum	$(\rho w'q')_o$	$-(\rho w'q')_h$	$-h\tilde{\rho}(\tilde{c}-\tilde{e})$	
	(10^{-3} g m^{-2} s^{-1})							
Around ice edge	−45	16	5	−24	40	−2	−14	
30–150 km	−44	16	−6	−34	63	−2	−27	
150–300 km	−2	5	−22	−19	69	−2	−48	
>300 km	−13	26	−20	−7	51	∼0	−44	
	$-\frac{\partial}{\partial x}(h\tilde{\rho}\tilde{u}\tilde{l})$	$(\rho ul)_h\frac{\partial h}{\partial x}$	$-(\rho wl)_h$	Sum	$h\tilde{\rho}(\tilde{c}-\tilde{e})$	$-h\tilde{\rho}\tilde{r}$		
	(10^{-3}g m^{-2} s^{-1})							
Around ice edge	−4	0	−0	−4	14	−10		
30–150 km	−5	0	−2	−7	27	−20		
150–300 km	1	0	−10	−9	48	−39		
>300 km	0	−0	−10	−10	44	−34		
	$-\frac{\partial}{\partial x}(h\tilde{\rho}\tilde{u}\tilde{\theta})$	$(\rho u\theta)_h\frac{\partial h}{\partial x}$	$(\rho w\theta)_h$	Sum	$(\rho w'\theta')_o$	$-(\rho w'\theta')_h$	$\frac{L}{c_p}h\tilde{\rho}(\tilde{c}-\tilde{e})$	$\frac{1}{c_p}(R_h-R_o)$
	(g K m^{-2} s^{-1})							
Around ice edge	−15 284	10 969	4247	−341	167	130	40	4
30–150 km	−7172	8929	−2146	−389	213	105	71	0
150–300 km	1211	3764	−5297	−322	164	50	123	−15
>300 km	741	5813	−6776	−222	85	42	112	−17

into account that the composite intervals for 150–300 km and greater than 300 km are represented by only three budget boxes each resulting in less confidence than for the other two intervals, which are represented by eight budget boxes each.

In the mass budget systematic variations in downstream direction are obvious: a decrease of the entrainment velocity w_e and an increase of the mean vertical motion from subsidence (over the ice-edge region) to rising motion over the water. These systematic variations are of course also present in the variations of the large-scale flow terms of the budgets of water vapor, water, and temperature. The net effect of the large-scale flow is always negative—that is, water vapor, water, and heat are exported—but with decreasing tendency in downstream direction, at least as far as water vapor and heat are concerned.

Both surface fluxes of moisture and heat increase from the ice-edge region to the open water. Farther downstream the heat flux decreases continuously, whereas the moisture flux reaches its maximum here. This results into a monotonic decrease of the so-called Bowen ratio B, defined as the ratio between the surface sensible heat flux $c_p(\rho w'\theta')_o$ and the surface latent heat flux $L(\rho w'q')_o$ from values larger to values smaller than one (Table 8). Note that on the global scale the smaller values of B are found over the subtropical and tropical oceans, where B is about 0.1–0.2. The strong systematic variation of B in CAOs implies that a constant B in order to estimate the latent heat flux from the sensible heat flux is not a good assumption.

Both condensation and precipitation increase in downstream direction, whereas the entrainment heat flux decreases systematically. Apart from the Bowen ratio other ratios of some important terms in the budget equations of q, l, and θ are presented in Table 8. The amount of water vapor condensed, $h\tilde{\rho}(\tilde{c}-\tilde{e})$, in relation to the amount of water vapor supplied from the sea surface, $(\rho w'q')_o$, continuously increases with x. The ratio is nearly twice as large (about 0.8) in the region of deeper cellular convection than (about 0.4) in the region of shallower longitudinal convection patterns. On the other hand, the efficiency with which condensed water is converted to precipitation, that is, the ratio $h\tilde{\rho}\tilde{r}/[h\tilde{\rho}(\tilde{c}-\tilde{e})]$,

Downloaded from http://journals.ametsoc.org/mwr/article-pdf/125/8/1824/4178812/1520-0493(1997)125_1824_blmwah_2_0_co_2.pdf by guest on 30 November 2020

TABLE 8. Ratios of various terms in the budgets of water vapor, water, and potential temperature calculated from the composite budgets in Table 7. The ratios are (from left to right column): net condensation versus surface water vapor flux, precipitation rate versus net condensation rate, precipitation rate versus surface water vapor flux, entrainment temperature flux versus surface temperature flux, net condensation heating versus surface sensible heat flux, and surface sensible versus surface latent heat flux.

	$\frac{h\tilde{\rho}(\tilde{c}-\tilde{e})}{(\rho w'q')_o}$	$\frac{h\tilde{\rho}\tilde{r}}{h\tilde{\rho}(\tilde{c}-\tilde{e})}$	$\frac{h\tilde{\rho}\tilde{r}}{(\rho w'q')_o}$	$\frac{(\rho w'\theta')_h}{(\rho w'\theta')_o}$	$\frac{L/c_p h\tilde{\rho}(\tilde{c}-\tilde{e})}{(\rho w'\theta')_o}$	$\frac{c_p(\rho w'\theta')_o}{L(\rho w'q')_o}$
Around ice edge	0.35	0.72	0.25	0.78	0.24	1.49
30–150 km	0.43	0.74	0.32	0.49	0.33	1.21
150–300 km	0.70	0.81	0.57	0.30	0.75	0.85
>300 km	0.86	0.77	0.66	0.49	1.32	0.59

is about the same in both regions with values around 0.75. Thus, the efficiency of precipitation production in relation to the surface water vapor flux—that is, the ratio $h\tilde{\rho}\tilde{r}/(\rho w'q')_o$—also increases, namely, from about 0.3 to 0.6.

The ratio between the entrainment heat flux $(\rho w'\theta')_h$ and the surface heat flux $(\rho w'\theta')_o$ is relatively high around the ice edge, where the boundary layer increases rapidly, and reduces to values around 0.4 at larger distances x. Here, the condensation is the dominating heating term in the heat budget, whereas farther upstream to a larger extent the surface flux and to a lesser extent the entrainment flux are dominating the heat supply, which is necessary to compensate the cooling by cold-air advection. The ratio of the net condensation heating, $L/c_p h\tilde{\rho}(\tilde{c}-\tilde{e})$, versus the surface flux heating $(\rho w'\theta')_o$ increases from 0.25 around the ice edge to values near 1.3 at distances of more than 300 km farther downstream. Heat budget calculations by Bond and Fleagle (1988) in situations of cellular convection behind a cold front over the Pacific Ocean also show that the heating by condensation was larger than by the surface heat flux.

b. Convective cloud patterns and physical processes

Table 6 shows that the classification with respect to the distance from the ice edge applies approximately also to a classification with respect to the convective pattern type. It may be presumed, therefore, that the systematic variations of the various terms in the budgets of water vapor, water, and temperature in downstream direction likewise represent systematic differences concerning the importance or relative importance of the various physical processes in regions of roll-like and cellular-like convection. The most obvious difference between both regions is the relative importance of the heat supply from the surface flux and by the condensation process in the clouds (Tables 7 and 8). If the above presumption is correct it may be concluded that cellular convection patterns will not occur unless the condensation heating has reached a certain amount, say, the magnitude of the surface sensible heat flux, as it is suggested by the ratio $L/c_p h\tilde{\rho}(\tilde{c}-\tilde{e})/(\rho w'\theta')_o$ in Table 8. On the other hand, the condensation heating cannot increase at will but is limited by the surface latent heat flux. Therefore, if we substitute $h\tilde{\rho}(\tilde{c}-\tilde{e})$ by its maximum possible value, namely, $(\rho w'q')_o$, then the criterion for the occurrence of cellular convection is related to the reciprocal value of the Bowen ratio B. Based on the B values listed in Table 8 it may be assumed that the critical Bowen ratio B_{crit} is on the order of 0.6 to 0.5.

It is supposed that $B < B_{\text{crit}}$ applies for deep cellular convection with cloud-layer depths of at least 1 km. At least the above criterion is in accordance with other observations of cellular convection in CAOs as, for example, reported by Agee and Dowell (1974), Hein and Brown (1988), Bond and Fleagle (1988), and Brümmer et al. (1986). It is not clear to what extent such a criterion holds for cellular convection in general, that is, also for shallow cellular convection as, for example, for situations with cellular structures in stratocumulus layers. It has to be investigated whether the relative value of condensation heating versus surface sensible heat flux is the only important condition for the occurrence of cellular convection or whether the absolute value of condensation heating is an important parameter as well. Therefore, the above estimated B_{crit} can be regarded only as a necessary but not a sufficient condition for the occurrence of deep cellular convection.

In a recent paper, Müller (1995) studied the importance of various physical processes for the generation of convection with large aspect ratios (defined as the ratio of horizontal cell diameter versus vertical cell depth h) in CAOs. By means of sensitivity studies with a large-eddy simulation (LES) model he found that condensation is an important process for the occurrence of convection with large aspect ratios of 10 or more. This result agrees with our findings. Furthermore, he found that cloud-top longwave radiational cooling is also a process advancing the generation of large-aspect-ratio convection. This is not supported by our findings. However, it should be mentioned that our radiation observations are relatively uncertain. Latent heat release due to condensation in cloud updrafts as a mechanism by which cellular convection can obtain its large aspect ratios has been investigated by many authors (e.g., Bjerknes 1938; van Delden 1987). In these analytical models

Downloaded from http://journals.ametsoc.org/mwr/article-pdf/125/8/1824/4178812/1520-0493(1997)125_1824_blmwah_2_0_co_2.pdf by guest on 30 November 2020

it was assumed that all condensed water in the updraft rains out and that the downdraft is dry and stable. Our estimate of 0.75 for the ratio of precipitation rate versus condensation rate shows that this assumption is not too unrealistic.

7. Summary and concluding remarks

Eleven cold-air outbreaks from the Arctic sea ice to the open water of the Fram Strait and the Norwegian Sea have been monitored by aircraft during the field campaigns ARKTIS 1993 and ARKTIS 1991. The measurements were made at places ranging from the ice-edge zone to several hundred kilometers farther downstream. Based on these data budgets of mass, water vapor, water, and heat have been calculated for 22 boxes within the atmospheric boundary layer. Under the assumption of stationarity and homogeneity in crosswind direction the individual terms of the budget equations (2a)–(2d) are computed directly from the data or as residue. The residual terms were the mean vertical mass flux at the top of the boundary layer, the condensation rate in clouds, the precipitation rate, and the entrainment heat flux.

The results for the individual CAOs show in most cases similar variations of the budget terms in downstream direction. In general, there is a trend in the mean vertical motion from subsidence near the ice edge zone toward mean upward motion at larger distances. Water vapor is supplied by evaporation at the sea surface, whereas the large-scale flow and the condensation in clouds remove water vapor from the boundary layer. Both evaporation at the surface and condensation in clouds increase in downstream direction as well as the ratio of condensation versus evaporation. Most of the water condensed, namely, about 0.75, falls as precipitation. This ratio is fairly constant with increasing distance x. The estimated precipitation rate thus increases on average from about 1 mm day^{-1} over the ice edge zone to 3–4 mm day^{-1} at distances of about 300 km.

In the heat budget, the heat export by the large-scale flow is compensated by heat supplied from the sea surface, by entrainment of warm inversion layer air into the boundary layer, by latent heat release due to condensation in clouds, and possibly by radiation flux divergence. The relative importance of these heat sources changes systematically with increasing distance x. At near distances from the ice edge, the surface and entrainment heat flux are dominating. The latent heat release is here small but increases downstream due to the increasing depth of the cloud and boundary layer. At distances of more than 300 km, where the cloud layer is more than 1 km deep, the latent heat release is the dominating heating term, followed by the surface heat flux whereas the entrainment flux plays no important role.

The boundary layer modification in CAOs goes parallel with the systematic transition of convection patterns from roll-like to cellular structures. In the region of cellular patterns the latent heat release in clouds is the dominating source in the heat budget of the boundary layer. A critical Bowen ratio of 0.5–0.6 was estimated to separate the regions of rolls and cells. This is probably a necessary but not a sufficient condition for the occurrence of cellular convection. Other parameters than the ratio of latent heat release versus surface heat flux play an important role for the convective structure selection as, for example, the profile shape of the wind components in crosswind direction (inflection point; e.g., Lilly 1966) and alongwind direction (curvature; e.g., Kuettner 1971).

Estimates of the budgets of mass, water vapor, water, and heat in the boundary layer at different distances from the ice edge during wintertime Arctic cold-air outbreaks have been performed in this paper for the first time to the author's knowledge. Although some terms in the budget equations could not be derived directly from the measurements but had to be derived as residues and consequently contain all possible uncertainties, the high degree of similarity of the budget results calculated independently for the individual CAOs on one hand and the reasonable downstream variation of individual terms in the budget equations on the other hand give much confidence in the overall validity of the derived results and conclusions. In this way quantitative estimates of the importance of the various physical processes causing the boundary layer modification in CAOs could be obtained.

Acknowledgments. The author thanks his colleagues B. Busack and B. Löbe for their support in the data processing, M. Lüdicke for drafting the figures, S. Lehmann for typing the manuscript, and two anonymous reviewers for their helpful comments. The study was supported by the German Science Foundation under Grant SFB 318, ''Processes relevant to climate in the atmosphere–ocean–cryosphere system.''

REFERENCES

Agee, E., and K. E. Dowell, 1974: Observational studies of mesoscale cellular convection. *J. Appl. Meteor.,* **13,** 46–53.

——, and F. Lomax, 1978: Structure of the mixed layer and inversion layer associated with patterns of mesoscale cellular convection during AMTEX 75. *J. Atmos. Sci.,* **35,** 2281–2301.

Atlas, D., B. A. Walter, S.-H. Chou, and P. J. Sheu, 1986: The structure of the unstable marine boundary layer viewed by lidar and aircraft observations. *J. Atmos. Sci.,* **43,** 1301–1318.

Bechthold, P., C. Fravalo, and J. P. Pinty, 1992: A study of a two-dimensional cloudiness transition during a cold-air outbreak event. *Bound.-Layer Meteor.,* **60,** 243–270.

Bjerknes, J., 1938: Saturated ascent of air through a dry adiabatically descending environment. *Quart. J. Roy. Meteor. Soc.,* **64,** 325–330.

Bond, N., and R. Fleagle, 1988: Prefrontal and postfrontal boundary layer processes over the ocean. *Mon. Wea. Rev.,* **116,** 1257–1273.

Brümmer, B., Ed., 1992: ARKTIS 199l: Report on the field phase with examples of measurements. Berichte aus dem Zentrum für

Downloaded from http://journals.ametsoc.org/mwr/article-pdf/125/8/1824/4178812/1520-0493(1997)125_1824_blmwah_2_0_co_2.pdf by guest on 30 November 2020

Meeres- und Klimaforschung, Reihe A, Nr. 3, 216 pp. [Available from Meteorological Institute, University of Hamburg, Budesstr. 55, D-20146 Hamburg, Germany.]

——, Ed., 1993: ARKTIS 1993: Report on the field phase with examples of measurements. Berichte aus dem Zentrum für Meeres- und Klimaforschung, Reihe A, Nr. 11, 270 pp. [Available from Meteorological Institute, University of Hamburg, Budesstr. 55, D-20146 Hamburg, Germany.]

——, 1996: Boundary layer modification in wintertime cold-air outbreaks from the Arctic sea ice. *Bound.-Layer Meteor.,* **80,** 109–125.

——, T. Fischer, and S. Zank, 1986: Aircraft observations of open cellular structures during KonTur. *Contrib. Atmos. Phys.,* **59,** 162–184.

——, B. Rump, and G. Kruspe, 1992: A cold-air outbreak near Spitsbergen in springtime—Boundary layer modification and cloud development. *Bound.-Layer Meteor.,* **61,** 13–46.

Chlond, A., 1992: Three-dimensional simulation of cloud street development during a cold-air outbreak. *Bound.-Layer Meteor.,* **58,** 161–200.

Chou, S.-H., and J. Zimmermann, 1989: Bivariate conditional sampling of buoyancy flux during an intense cold-air outbreak. *Bound.-Layer Meteor.,* **46,** 93–112.

Curry, J. A., F. G. Meyer, L. F. Radke, C. A. Brock, and E. E. Ebert, 1990: Occurrence and characteristics of lower tropospheric ice crystals in the Arctic. *Int. J. Climate,* **10,** 749–764.

Etling, D., and S. Raasch, 1987: Numerical simulations of vortex roll development during a cold-air outbreak. *Dyn. Atmos. Oceans,* **10,** 277–290.

Fiedler, B., 1984: The mesoscale stability of entrainment into cloud-topped mixed layers. *J. Atmos. Sci.,* **41,** 92–101.

Hein, P., and R. A. Brown, 1988: Observations of longitudinal roll vortices during Arctic cold-air outbreaks over open water. *Bound.-Layer Meteor.,* **45,** 177–199.

Helfand, M., and E. Kalnay, 1983: A model to determine open and closed cellular convection. *J. Atmos. Sci.,* **40,** 631–650.

Kuettner, J. P., 1971: Cloud bands in the atmosphere. *Tellus,* **23,** 404–425.

Lilly, K. D., 1966: On the stability of Ekman boundary flow. *J. Atmos. Sci.,* **23,** 451–494.

Müller, G., 1995: Mesoskalige Zellularkonvektion in Abhängigkeit von unterschiedlichen physikalischen Prozessen und synoptischen Randbedingungen—Numerische Simulationen. Ph.D. dissertation, University of Hamburg, 144 pp. [Available from Meteorological Institute, University of Hamburg, Budesstr. 55, D-20146 Hamburg, Germany.]

Ninomiya, K., and T. Akiyama, 1976: Structure and heat energy budget of mixed layer capped by inversion during a period of polar outbreak over Kuroshio region. *J. Meteor. Soc. Japan,* **54,** 160–174.

Sheu, P.-J., and E. Agee, 1977: Kinematic analysis and air–sea flux associated with mesoscale cellular convection during AMTEX 75. *J. Atmos. Sci.,* **34,** 793–801.

Stage, S., and J. Businger, 1981: A model for entrainment into a cloud-topped marine boundary layer. Part I: Model description and application to a cold-air outbreak episode. *J. Atmos. Sci.,* **38,** 2213–2229.

Stull, R. B., 1988: *An Introduction to Boundary Layer Meteorology*. Kluwer Academic Publishers, 666 pp.

Sun, W.-Y., and W.-R. Hsu, 1988: Numerical study of a cold-air outbreak over the ocean. *J. Atmos. Sci.,* **45,** 1205–1227.

——, and A. Yildirim, 1989: Air mass modification over Lake Michigan. *Bound.-Layer Meteor.,* **48,** 345–360.

van Delden, A., 1987: On cumulus cloud patterns and the theory of shallow convection. Ph.D. dissertation, University of Utrecht, 185 pp.

Walter, B. A., 1980: Wintertime observations of roll clouds over the Bering Sea. *Mon. Wea. Rev.,* **108,** 2024–2031.

——, 1986: The mesoscale organization, dynamics, and evolution of the marine planetary boundary layer during cold-air outbreaks. Ph.D. dissertation, University of Washington, 200 pp. [Available from University Microfilms, 300 North Zeeb Rd., Ann Arbor, MI 48106.]

Wayland, R., and S. Raman, 1989: Mean and turbulent structure of a baroclinic marine boundary layer during the 28 January 1986 cold-air outbreak (GALE 86). *Bound.-Layer Meteor.,* **48,** 227–254.

Yuen, C.-W., 1985: Simulations of cold surges over oceans with applications to AMTEX 75. *J. Atmos. Sci.,* **42,** 135–154.

Downloaded from http://journals.ametsoc.org/mwr/article-pdf/125/8/1824/4178812/1520-0493(1997)125_1824_blmwah_2_0_co_2.pdf by guest on 30 November 2020